Available online at www.sciencedirect.com
ScienceDirect
Trans. Nonferrous Met. Soc. China 31(2021) 111−124
Transactions of Nonferrous Metals Society of China
www.tnmsc.cn

Microstructure, mechanical properties and corrosion behavior of quaternary Mg−1Zn−0.2Ca−*x*Ag alloy wires applied as degradable anastomotic nails

Ying-zhong MA[1], De-xin WANG[1], Hong-xiang LI[1], Chang-lin YANG[2], Fu-song YUAN[3], Ji-shan ZHANG[1]

1. State Key Laboratory for Advanced Metals and Materials,
University of Science and Technology Beijing, Beijing 100083, China;
2. State Key Laboratory of Solidification Processing, Northwestern Polytechnical University, Xi'an 710072, China;
3. Center of Digital Dentistry, Peking University Hospital of Stomatology, Beijing 100081, China

Received 1 March 2020; accepted 29 September 2020

Abstract: The microstructure, mechanical properties and corrosion behavior of quaternary degradable Mg−1Zn−0.2Ca−*x*Ag (*x*=1, 2, 4 wt.%) alloy wires, intended as anastomotic nails, were investigated. It was found that these Ag-containing alloy wires mainly consist of Mg matrix and $Ag_{17}Mg_{54}$ phase, characterized by SEM, EDS, XRD and TEM. Tensile and knotting tests results demonstrate the superior mechanical properties of these alloy wires. Especially, Mg−1Zn−0.2Ca−4Ag alloy exhibits the highest mechanical properties, i.e. an ultimate tensile strength of 334 MPa and an elongation of 8.6%. Moreover, with increasing Ag content, the corrosion rates of these alloy wires remarkably increase due to the formation of more micro-galvanic coupling between Mg matrix and $Ag_{17}Mg_{54}$ phase, shown by mass loss and scanning Kelvin probe force microscopy (SKPFM) results. The present alloy can be completely degraded within 28 d, satisfying the property requirements of anastomotic nails.

Key words: Mg−Zn−Ca−Ag alloy; degradability; anastomotic nails; microstructure; mechanical properties; corrosion behavior

1 Introduction

Biodegradable Mg alloys are promising as candidates for medical applications due to their extraordinary properties such as high specific strength, high specific stiffness, low density, adaptable degradability and good biocompatibility [1−4]. It is estimated that the Mg amount consumed by an adult is 300−400 mg/d, and the excess can be excreted through metabolism [5]. The application of magnesium stents implanted in human body also confirms the biosafety of Mg or its alloys as medical materials [6].

Currently, biodegradable Mg alloys are attaining excellent application prospects in cardiovascular or orthopaedic devices such as vascular stents and bone-screws, and more and more studies are also being focused on these fields [7−9]. In the orthopaedic field such as gastrointestinal anastomosis surgery, Mg and its alloys are also playing a very significant role as an anastomotic nail material. Compared with the traditional pure titanium or its alloy wires, the degradable Mg metal wires can avoid second surgery, decrease infection chance, and prohibit anastomotic restenosis [4,10,11]. However, so far, few studies have aimed at Mg or its alloy wires, which are typically fabricated through hot or cold

Corresponding author: Hong-xiang LI, Tel: +86-10-62332350, E-mail: hxli@skl.ustb.edu.cn;
Ji-shan ZHANG, Tel: +86-10-62334717, E-mail: zhangjs@skl.ustb.edu.cn
DOI: 10.1016/S1003-6326(20)65481-4
1003-6326/© 2021 The Nonferrous Metals Society of China. Published by Elsevier B.V. & Science Press

drawing process [12−14]. Meanwhile, as the nail materials, some problems still need to be solved. For example, CAI et al [15] fabricated the Mg−2Zn alloy with an ultimate tensile strength up to 250 MPa and an elongation above 10% via cold drawning and heat treatment, currently being applied as the anastomotic nail materials. The extruded Mg−6Zn alloy prepared by ZHANG et al [16] exhibited an ultimate tensile strength of 279.5 MPa which is still not enough as the biodegradable anastomotic nails. Moreover, the Mg−6Zn wires cannot degrade in vivo within a few weeks, which cannot exhibit the advantages of degradable metals completely [16,17]. Therefore, finding an adaptable degradable magnesium alloy wire with better mechanical properties and faster degradable rate is necessary for the widespread application of anastomotic nails in the future.

The Mg−Zn−Ca alloys were confirmed to be a good candidate applied as an anastomotic nail material, which has been investigated in our previous researches [18−20]. Ca and Zn are the elements of biosafety and biodegradability, and they can be metabolized in a human body reported by NAMI et al [21] and SUN et al [22]. However, the properties of these alloys are still not enough to satisfy the requirements of anastomotic nail materials, especially the degradable rate and the mechanical properties. Thus, it is necessary to promote further development of Mg−Zn−Ca alloys.

Ag is an important trace element with a good biological safety in human body and Ag ion has bactericidal effect and prevents bacteria from attaching to Ag surface. In recent years, Ag has been successfully applied in wound healing and implant field [23,24]. On the other hand, Ag addition is also beneficial to refining grains, improving strength and accelerating degradation reaction [25,26]. However, it is known that the current researches mainly focus on Mg−Ag binary alloys or Mg−Ag−X ternary alloys [27−30]. Currently, Ag is seldom investigated in quaternary magnesium alloys, especially lacking the corresponding report on the effect of Ag addition on the microstructure, mechanical properties and corrosion behaviors of the magnesium alloy wires, although these alloy wires can be very promising as the anastomotic nail materials.

For this aim, quaternary Mg−1Zn−0.2Ca−*x*Ag alloy wires with different Ag contents were designed and prepared by extrusion and cold drawing in this study. The mechanical properties were evaluated by stretching and knotting tests, and the immersion, hydrogen evolution and electrochemical experiments were conducted to investigate the corrosion behaviors. The mechanisms on improving mechanical properties and influencing the corrosion behaviors by Ag addition were also discussed in detail.

2 Experimental

2.1 Material preparation

Mg−1Zn−0.2Ca−*x*Ag (*x*=1, 2, 4 wt.%) alloy ingots were prepared with pure Mg (99.99 wt.%), pure Zn (99.99 wt.%), pure Ag (99.99 wt.%) and Mg−20wt.%Ca master alloy, and melting was conducted at 700−750 °C in an electric resistance furnace under the protection of CO_2 (99 vol.%) and SF6 (1 vol.%). The melt was stirred and held for about 15 min and cast into a steel mold with a diameter of 85 mm and a height of 100 mm at 700 °C. The ingots were extruded into the alloy rods with a diameter of 16 mm at 340−360 °C with an extrusion ratio of 28:1 and an extrusion rate of 6 mm/s. The continuous multi-pass cold drawing at room temperature was used to achieve fine alloy wires and the deformation amount per pass was about 10%. The drawing angle in the die was about 7°. As a result, the magnesium alloy wires with a diameter of 0.5 mm were attained and then these magnesium alloy wires were annealed at 240 °C for 30 min. The chemical compositions of the alloy wires are listed in Table 1.

2.2 Characterization of microstructure and mechanical properties

The alloy wires for the microstructure characterization were cut from the longitudinal sections and cold-mounted in epoxy resin. Then, the samples were ground on SiC papers up to 2000 grit and then polished to mirror-like surface with 0.5 μm

Table 1 Actual compositions of magnesium alloy wires (wt.%)

Alloy	Zn	Ca	Ag	Mg
Mg−1Zn−0.2Ca−1Ag	0.90	0.11	0.84	Bal.
Mg−1Zn−0.2Ca−2Ag	0.80	0.10	1.60	Bal.
Mg−1Zn−0.2Ca−4Ag	0.94	0.12	3.54	Bal.

diamond polishing paste. Morphologies of magnesium alloy wires were observed by a scanning electron microscope (SEM) (Phenom XL, Finland) equipped with energy-dispersive an X-ray spectroscope (EDS). The precipitated phases of these alloy wires were examined by an X-ray diffractometer (XRD) with scanning angles ranging from 10° to 90° under the conditions of 40 kV and 40 mA. A detailed analysis of the second phase in the alloy wires was conducted using transmission electron microscope (TEM) and TEM samples were obtained by ion milling. The tensile tests were carried out using an electronic tensile testing machine and the tensile direction was parallel to the drawing direction of the wire with a gauge length of 140 mm at a strain rate of 5×10^{-5} s^{-1} and room temperature.

2.3 Corrosion test

The corrosion rates of alloy wires were calculated using mass loss in the simulated body fluid (SBF). The ratio of the SBF volume to the wire surface was 20:1 (mL/cm^2) according to ASTM-G31—72. The samples with a length of 30 mm and a diameter of 0.5 mm were used for the immersion test and at least three parallel samples per composition were evaluated. Specimens for immersion test were ultrasonic cleaned with acetone and absolute ethanol. All the alloy wires were rinsed with distilled water and dried in air after immersion and chromic acid solution (200 g/L CrO_3 + 10 g/L $AgNO_3$) was used to remove the surface corrosion product. The surface morphologies were also observed by SEM and the corrosion rates (mm/a) were calculated according to ASTM-G31—72.

The samples for electrochemical experiments were polished with 2000 grit silicon carbide paper, degreased with acetone and absolute ethanol, and cleaned with distilled water and finally dried in air. Electrochemical experiments were performed using a standard three-electrode system with a saturated calomel electrode as reference electrode, a platinum electrode as auxiliary electrode and the sample as working electrode with an exposure area of 0.316 cm^2 at 37 °C. The electrochemical impedance spectroscopy (EIS) analysis was conducted to monitor the corrosion behavior of alloy wires and the experiment was carried out by using an excitation voltage of 10 mV in the frequency ranging from 10^5 Hz to 10^{-2} Hz. The potentiodynamic polarization was monitored from −2 to −1 V at a scanning rate of 1 mV/s. The results were analyzed by Versa studio and ZsimpWin software. Scanning Kelvin probe force microscopy (SKPFM) was introduced to measure the relative potential between the second phase and the matrix α-Mg for further analyzing the corrosion mechanism of the Mg−Zn−Ca−Ag alloys.

The hydrogen generated by magnesium alloy wires was collected during the degradation process in SBF. The rate of hydrogen generation (v_H, mL/(cm^2·d)) was calculated based on the volume of hydrogen generated during the whole experimental period of hydrogen evolution. The corresponding corrosion rate was calculated (R_{corr}, mm/a) according to the following formula:

$$R_{corr}=2.279v_H \quad (1)$$

3 Results and discussion

3.1 Microstructure

The microstructures of the Mg−Zn−Ca−Ag alloy wires observed by optical microscope (OM) are shown in Fig. 1. It is noted that the grain size decreases to a very low level with the addition of Ag. The average sizes of the grains are 2.77, 2.50 and 2.27 μm for Mg−1Zn−0.2Ca−1Ag, Mg−1Zn−0.2Ca−2Ag and Mg−1Zn−0.2Ca−4Ag alloys, respectively. In addition, the grain size of Mg−1Zn−0.2Ca−4Ag alloy wire is more uniform than that of the other two wires. Some circular precipitates appear in alloy wires, and the precipitates gradually grow with the increase of Ag content. The precipitated phases are distributed at grain boundaries or in the matrix.

The representative SEM images of Mg−1Zn−0.2Ca−1Ag, Mg−1Zn−0.2Ca−2Ag and Mg−1Zn−0.2Ca−4Ag alloy wires are shown in Figs. 2(a)−(c), respectively. Some small spherical phases can be detected in these Ag-added alloy wires. The number of the second phase apparently increases when the Ag content increases. The Mg−1Zn−0.2Ca−4Ag alloy wires exhibit precipitates with a more quantity and a larger volume compared with Mg−1Zn−0.2Ca−1Ag and Mg−1Zn−0.2Ca−2Ag wires, as depicted in Fig. 2(c). EDS results confirm that these phases are mainly composed of Mg, Ag and Zn elements as shown in Figs. 2(d)−(f). The precipitated phases of the alloy wires are also

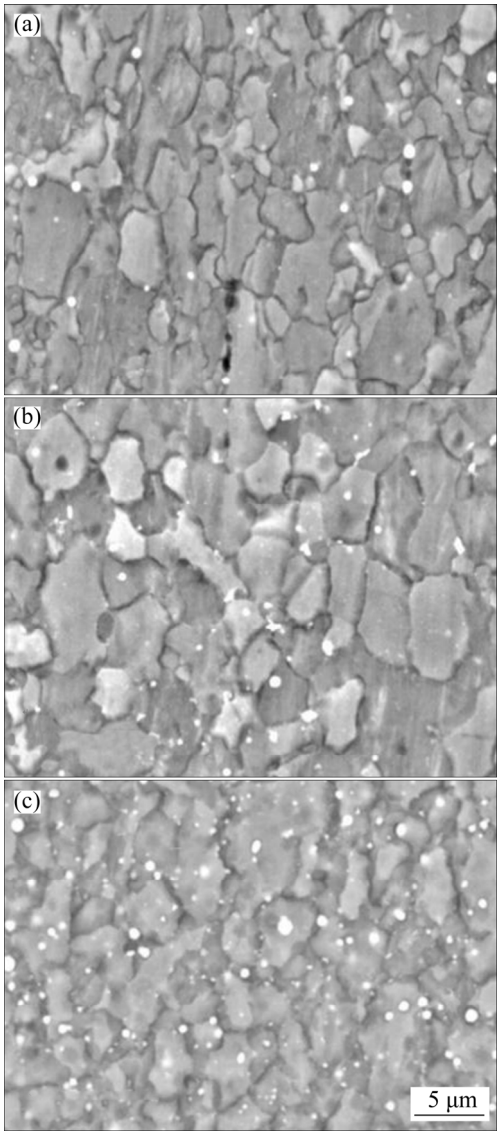

Fig. 1 OM images of Mg−1Zn−0.2Ca−1Ag (a), Mg−1Zn−0.2Ca−2Ag (b) and Mg−1Zn−0.2Ca−4Ag (c)

characterized by XRD, as depicted in Fig. 3. Strong intensity of matrix Mg (Mg has a hexagonal structure with lattice constants a=0.3209 nm and c=0.5211 nm) peaks are observed in these samples. The maximum solubility of Ag in Mg is less than 1% [31] and the solid solubility limit of Ca in Mg is 1.34% at room temperature in the equilibrium state [32]. Beyond solubility of the elements, the second phases are precipitated as illustrated by the XRD results. The precipitates in Mg−Zn−Ag ternary system can be defined to be $Ag_{17}Mg_{54}$ and $Mg_{51}Zn_{20}$ [33]. However, only $Ag_{17}Mg_{54}$ phase can be identified in the XRD spectrum as the main precipitates of the Mg−1Zn−0.2Ca−xAg alloy wires. The reason why $Mg_{51}Zn_{20}$ was not detected in the XRD patterns can be attributed to the dissolution of Zn into Mg matrix with the low addition of Zn in our study and the lower mixing enthalpy change of Mg−Zn (−4 kJ/mol) than that of Mg−Ag (−10 kJ/mol) [32]. This indicates that the Mg atoms bond more easily with the Ag than the Zn and Ca atoms.

Transmission electron microscope (TEM) was introduced to further determine the characteristics of precipitated phases. Figure 4 displays the TEM bright field images and the corresponding selected area electron diffraction (SAED) patterns for the Mg−1Zn−0.2Ca−1Ag and Mg−1Zn−0.2Ca−4Ag alloy wires. Some spherical precipitates can be observed from the TEM images. The oval precipitates shown in Fig. 4(a) are identified as $Ag_{17}Mg_{54}$ phase according to the SAED pattern of Fig. 4(b). The phase has an orthogonal structure with lattice constants a, b and c values of 1.4167, 1.4242 and 1.4693 nm, respectively. For the spherical phases of Mg−1Zn−0.2Ca−4Ag alloy wires displayed in Fig. 4(e), $Ag_{17}Mg_{54}$ phase can be identified by the SAED analysis taken with the electron beam parallel to [001] direction, as shown in Fig. 4(f). The above results strongly prove that the alloys have the same precipitated phases in the Ag-containing alloys. The ternary phase $Ca_2Mg_6Zn_3$ is discerned in Mg−Zn−Ca alloy system [34]. However, $Ca_2Mg_6Zn_3$ phase is not found in this study. An investigation discloses that the mixing enthalpy change of Mg−Zn (−4 kJ/mol) and Mg−Ca (−6 kJ/mol) is less than that of Mg−Ag (−10 kJ/mol) [32], manifesting that the Mg atoms bond with the Ag atoms more easily than the Zn and Ca atoms. In addition, for the Mg−1Zn−0.2Ca−1Ag alloy wires, the dislocations induced from the cold drawing deformation, keep at a low level, as seen in Fig. 4(c), while the corresponding dislocations are not observed in Mg−1Zn−0.2Ca−2Ag and Mg−1Zn−0.2Ca−4Ag alloy wires.

3.2 Mechanical properties

The knotting test is more complex than the tensile test and closer to the actual production. The knotting tests are aimed at evaluating the formability of the magnesium alloy wires and the results are displayed in Figs. 5(a)−(c). Four knots are made at the fixed positions of each wire, and then any fractures will be observed during the knotting process. In our research, fractures do not occur with knotting tests for the three wires,

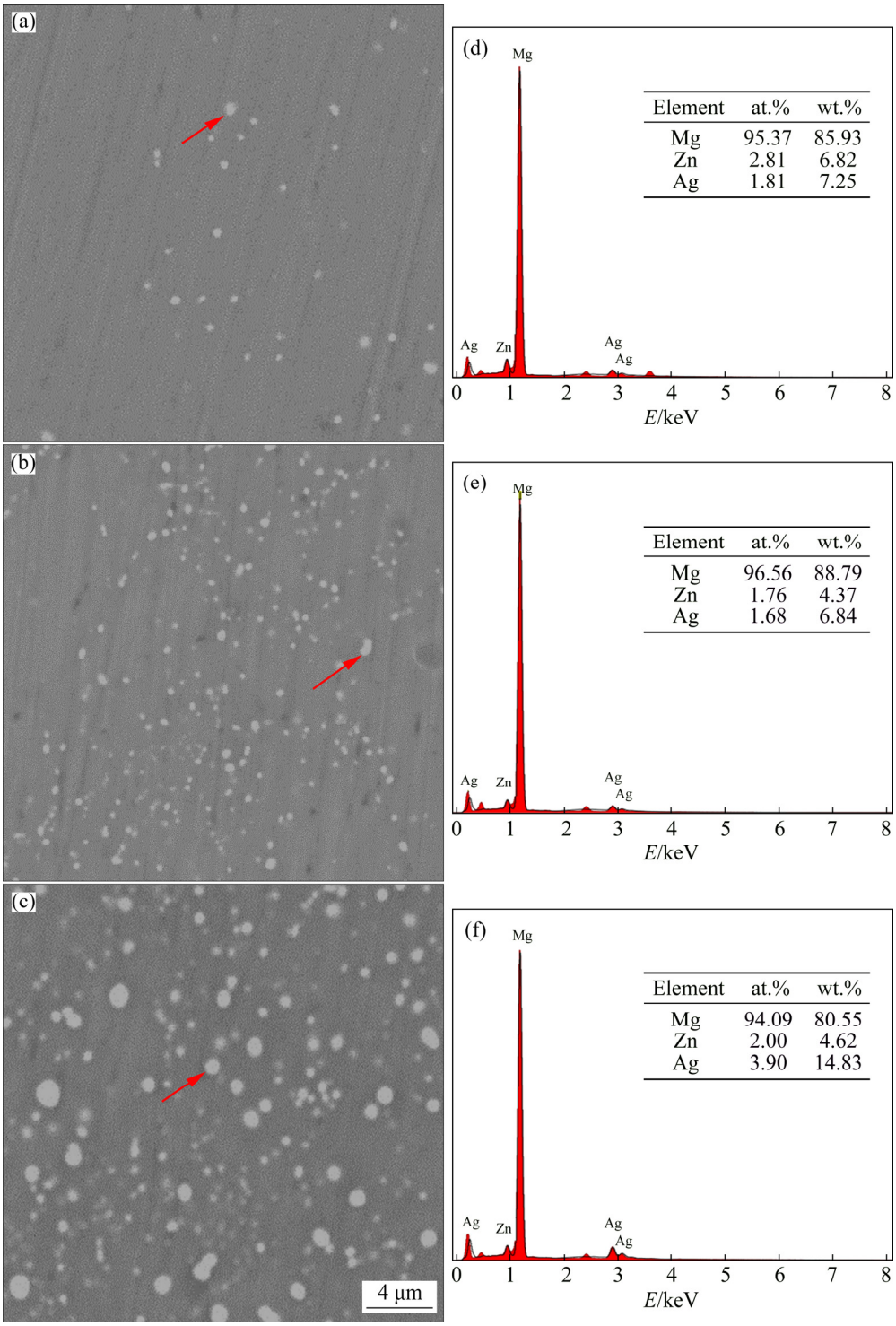

Fig. 2 SEM images (a−c) and EDS analysis results (d−f) of Mg−1Zn−0.2Ca−1Ag (a, d), Mg−1Zn−0.2Ca−2Ag (b, e) and Mg−1Zn−0.2Ca−4Ag (c, f)

confirming good plasticity of these alloy wires for anastomotic application. Furthermore, Fig. 5(d) shows the dependence of the mechanical properties of the Mg−1Zn−0.2Ca−*x*Ag alloy wires after annealing on the Ag content. All the alloy wires exhibit high tensile strength and medium plasticity. Ag has a significant impact on mechanical properties. The ultimate tensile strength (UTS) and yield strength (YS) decrease for the Mg−1Zn−0.2Ca−2Ag alloy wires and then increase when the addition of Ag reaches 4%, while the trend of elongation is just opposite against the strength.

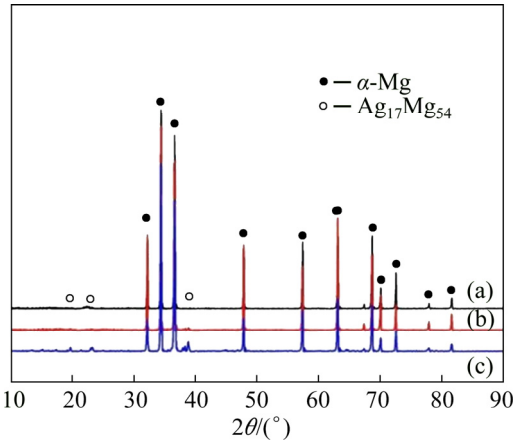

Fig. 3 XRD patterns of Mg−1Zn−0.2Ca−*x*Ag alloy wires: (a) Mg−1Zn−0.2Ca−1Ag; (b) Mg−1Zn−0.2Ca−2Ag; (c) Mg−1Zn−0.2Ca−4Ag

Mg−1Zn−0.2Ca−2Ag alloy wires have the maximum elongation of 8.9% with the lowest UTS of 313 MPa and YS of 264 MPa. Mg−1Zn−0.2Ca−4Ag alloy wires get the highest UTS of 334 MPa and YS of 292 MPa with a decent elongation of 8.6%. In general, the alloy remains a decent elongation of above 8% with the strength increasing. The current Mg−1Zn−0.2Ca−4Ag alloy wires exhibit much higher tensile strength than the Mg−2Zn [15] and Mg−6Zn [16] alloy wires, which are promising as the potential biodegradable materials of anastomotic nails instead of the current mainstream alloy wires.

The mechanical properties of magnesium alloys are affected by each alloying constituent. In this study, the size and number of precipitated

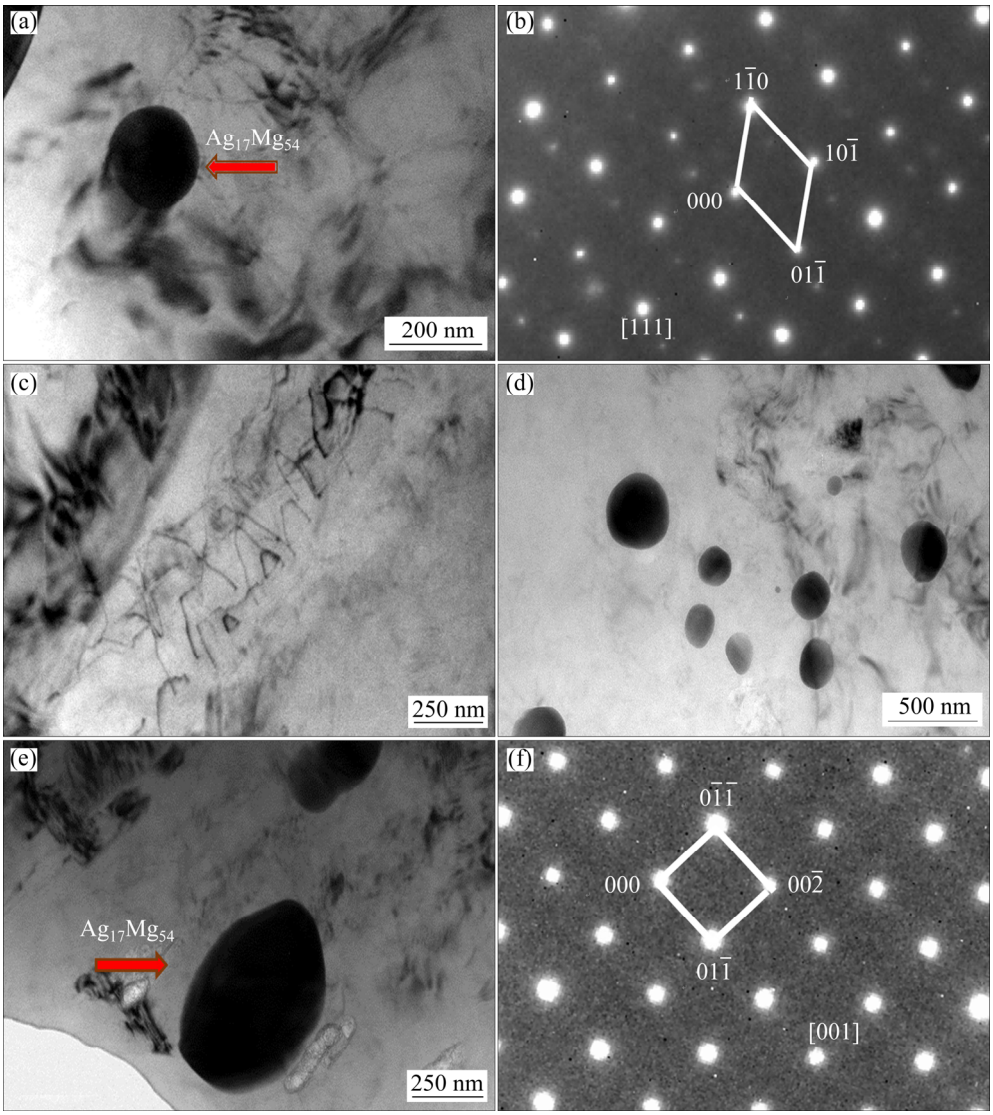

Fig. 4 TEM bright field images and SAED patterns of Mg−1Z0.2n−Ca−*x*Ag alloy wires: (a, c) TEM bright field images of Mg−1Zn−0.2Ca−1Ag alloy; (b) SAED pattern of $Ag_{17}Mg_{54}$ shown in (a); (d, e) TEM bright field images of Mg−1Zn−0.2Ca−4Ag alloy; (f) SAED pattern of $Ag_{17}Mg_{54}$ shown in (e)

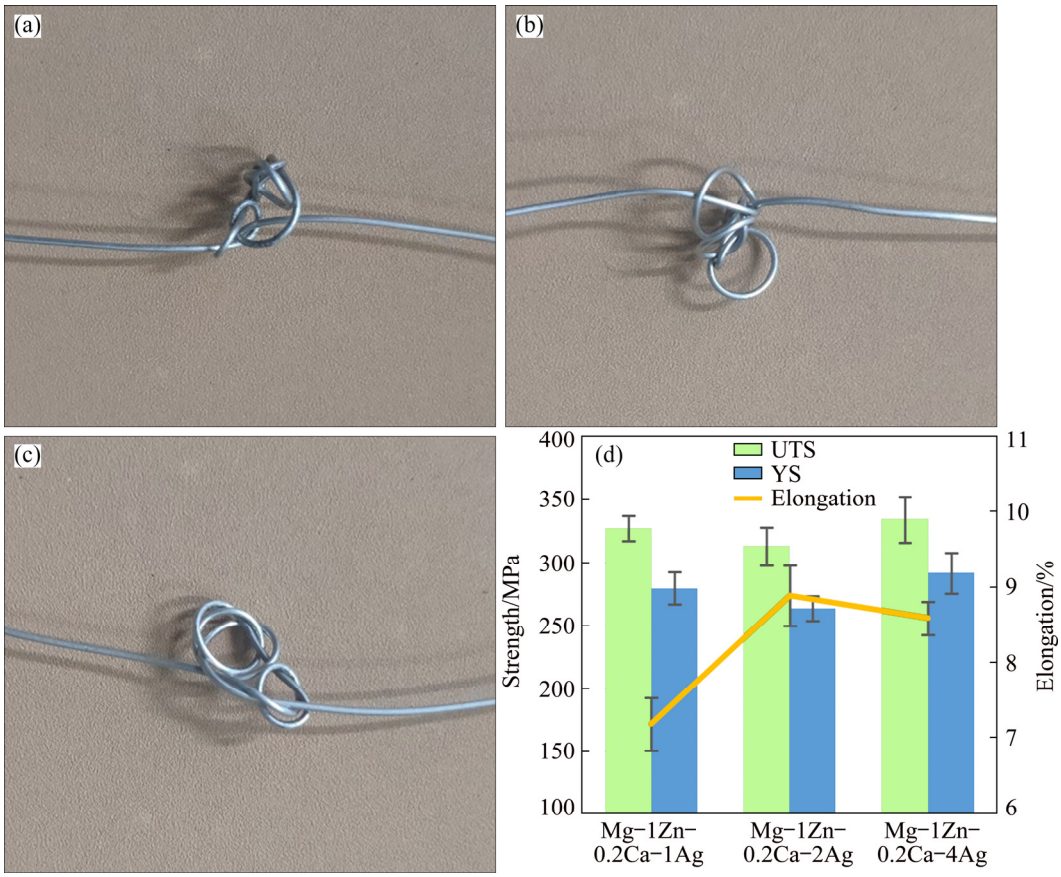

Fig. 5 Knotting test samples of Mg−1Zn−0.2Ca−1Ag (a), Mg−1Zn−0.2Ca−2Ag (b), Mg−1Zn−0.2Ca−4Ag (c) and mechanical properties of Mg−1Zn−0.2Ca−*x*Ag alloy wires after annealing (d)

phases increase significantly with the increase of Ag content. The adverse change in strength and plasticity indicates that both properties may not be improved simultaneously. From Mg−1Zn−0.2Ca−1Ag to Mg−1Zn−0.2Ca−4Ag, precipitation strengthening becomes more dominant when more and more second phases precipitate while the sizes of them also grow larger and larger. Also, grain refinement caused by Ag addition is more obvious for the Mg−1Zn−0.2Ca−4Ag alloy wires and as a result the mechanical properties can be improved due to the Hall−Petch rule, which is also reported by other researchers [35,36]. Other factors such as annealing texture and residual stress may also affect mechanical properties, which require further investigations in the future.

3.3 Corrosion properties

Surface morphologies of magnesium alloy wires before and after removal of corrosion products are displayed in Fig. 6. After being subjected to immersion, all the magnesium alloy wires are suffered severe corrosion with cracks, which is resulted from the evolution of hydrogen bubbles, the loss of corrosion products and the surface shrinkage. The existence of cracks accelerates the corrosion process via making the solution easier to contact the α-Mg matrix. The surface of Mg−1Zn−0.2Ca−4Ag alloy wire shows the most serious corrosion and lost most of its initial metallic luster, while Mg−1Zn−0.2Ca−1Ag and Mg−1Zn−0.2Ca−2Ag alloy wires seem to exhibit a relatively slight damage. Their corrosion surfaces of the alloys have small amounts of white corrosion products. The EDS results of Point *a* (Fig. 6(a)) and Point *b* (Fig. 6(e)) demonstrate that the white products are probably the $Mg(OH)_2$ due to the molar ratio of oxygen to magnesium. In general, the insoluble $Mg(OH)_2$ film acts as a barrier to strengthen the corrosion resistance of wires and prevents corrosion to a certain extent.

The results of hydrogen evolution are plotted in Fig. 7. It should be noted that an attractive characteristic of the Mg−1Zn−0.2Ca−4Ag alloy wires during immersion in aqueous solution is its active generation of H_2 gas in comparison with the

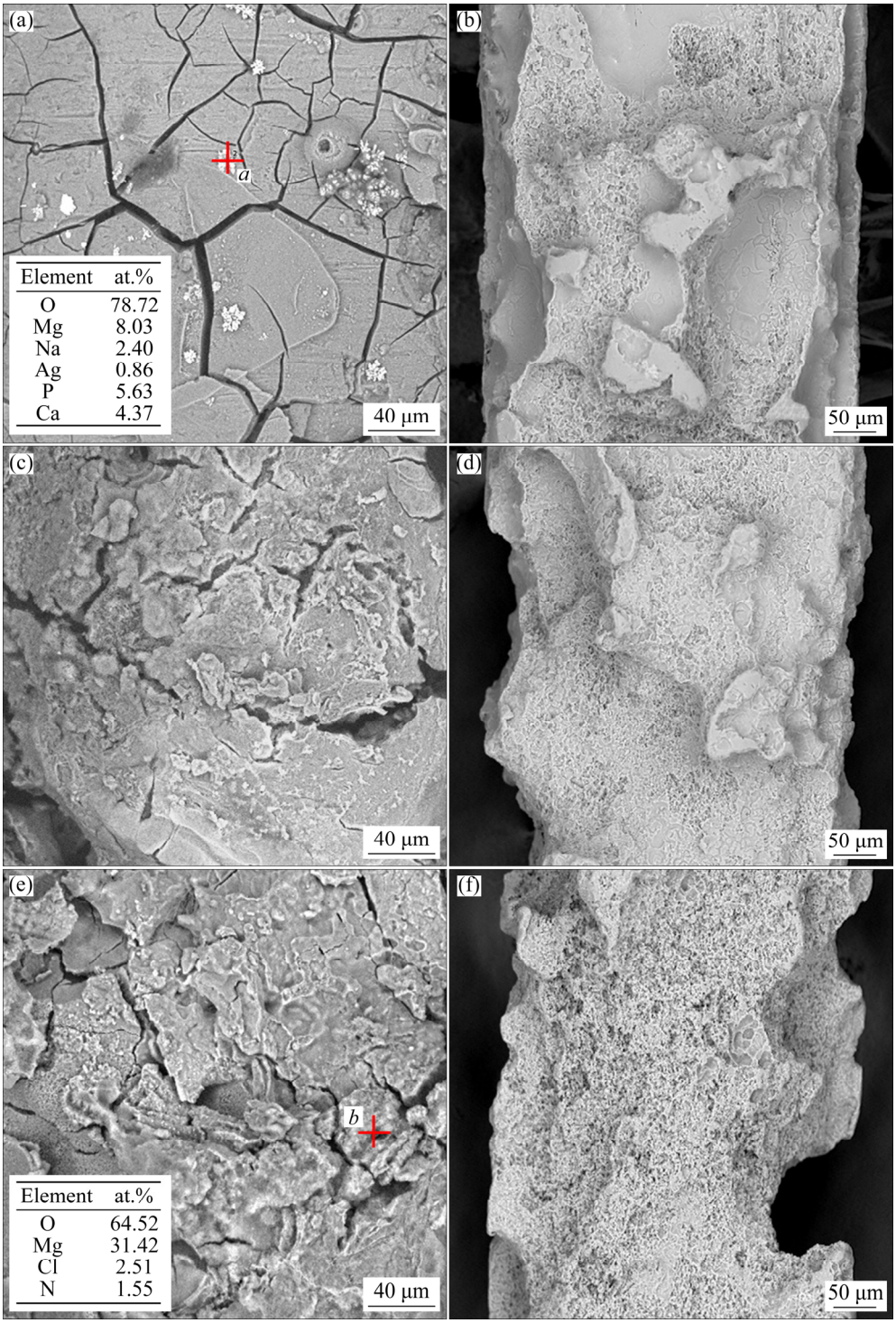

Fig. 6 Surface morphologies of Mg−1Zn−0.2Ca−1Ag (a, b), Mg−1Zn−0.2Ca−2Ag (c, d) and Mg−1Zn−0.2Ca−4Ag (e, f) alloys before and after removal of corrosion products, respectively

Mg−1Zn−0.2Ca−1Ag and Mg−1Zn−0.2Ca−2Ag alloy wires. The volume of hydrogen evolution increases with increasing immersion time. The hydrogen evolution rate is a little higher at the beginning of the experiment. However, the rate begins to slow down due to a protective film formed afterwards. The film retards the degradation and causes a decline in corrosion rate with time prolonging. The magnesium hydroxide product layer is insoluble in water, thus it precipitates on the surface and restrains the galvanic reaction between $Ag_{17}Mg_{54}$ phase and α-Mg matrix.

It is well-known that microstructural features such as grain size and the amount and distribution

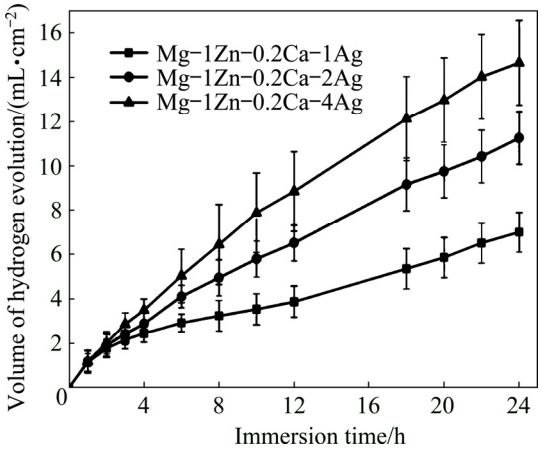

Fig. 7 Volume of hydrogen evolution of Ma−1Zn−0.2Ca−*x*Ag during 24 h immersion in SBF

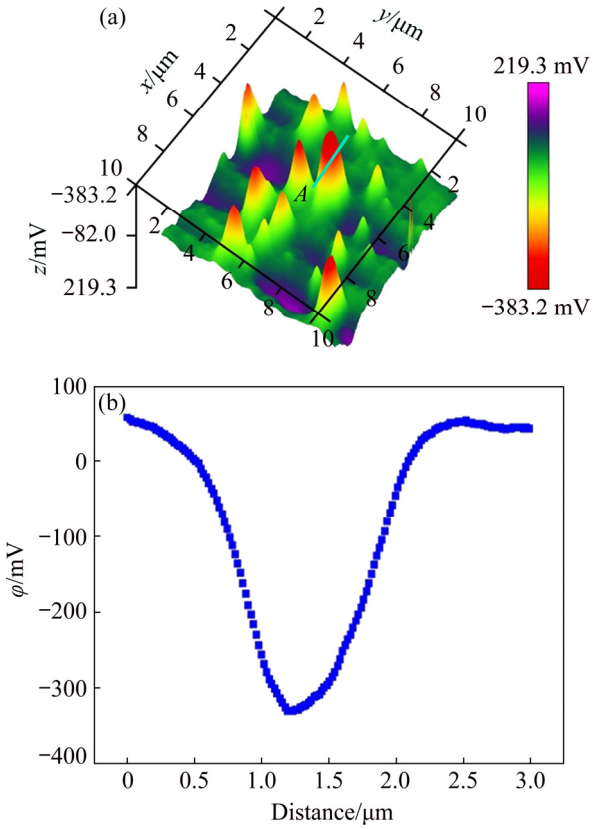

Fig. 8 3D potential diagram of Mg−1Zn−0.2Ca−4Ag (a) and potential profile (b) along line *A* in (a)

of the second phase in the magnesium alloys have important influences on corrosion resistance. Ag addition can reduce the mean grain size and the susceptibility to pitting corrosion gets passivated according to Ref. [28]. However, in this study, the quantity and distribution of the second phase may play a more predominant role in corrosion behavior of the alloys. Figure 8 shows the 3D potential map of Mg−1Zn−0.2Ca−4Ag from SKPFM for further analysis, which confirms that the potential of the second phase $Ag_{17}Mg_{54}$ is obviously lower than that of *α*-Mg matrix. The potential of *α*-Mg matrix has an average range of 50 mV and that of the second phase is only about −300 mV. Microstructure analysis confirms that the second phase of Mg−1Zn−0.2Ca−*x*Ag alloy wires is $Ag_{17}Mg_{54}$ and forms a micro-galvanic corrosion cell with *α*-Mg matrix. Moreover, the $Ag_{17}Mg_{54}$ phase can be regarded as an anode due to its low potential and will be corroded preferentially, while the *α*-Mg acts as a cathode. The micro-galvanic corrosion cell becomes larger and deeper along with the increase of Ag content because the second phase precipitates more and distributes widely as shown in Fig. 2. Although $Ag_{17}Mg_{54}$ is degraded firstly, the Mg matrix is protected to some extent. However, a dramatic increase of micro-galvanic corrosion causes a lot of corrosion holes which can connect into corrosion gully, thus the overall corrosion of the alloys is accelerated. The larger exposure areas contacted with aqueous solutions also improve the corrosion rate of Mg matrix so that the cavities are formed after dissolution of intermetallic phases, especially for Mg−1Zn−0.2Ca−4Ag alloy. Besides, more details on the degradation mechanism will be studied and discussed from the following electrochemical analysis.

Potentiodynamic polarization curves, as shown in Fig. 9(a), are determined using SBF solution as electrolyte to evaluate the degradable ability of Mg−1Zn−0.2Ca−*x*Ag alloys. The corrosion current density (J_{corr}) and corrosion potential (φ_{corr}) obtained by Tafel extrapolation are shown in Table 2. The addition of 2 wt.% Ag can lead to a shift in the corrosion potential to a more positive direction compared with Mg−1Zn−0.2Ca−1Ag alloy wire, while the negative shift is observed with Ag content reaching 4 wt.% compared with Mg−1Zn−0.2Ca−2Ag alloy wire.

EIS is also a widely used tool to monitor the corrosion process. Figures 9(b)−(d) show the Nyquist and Bode plots of the Mg−1Zn−0.2Ca−*x*Ag alloy wires in SBF. The capacitive loop in the high frequency region is related to the electrolyte conductivity through the corrosion product film, while the loop in the middle frequency region owes to the charge transfer reaction at the interface of the metal surface and the

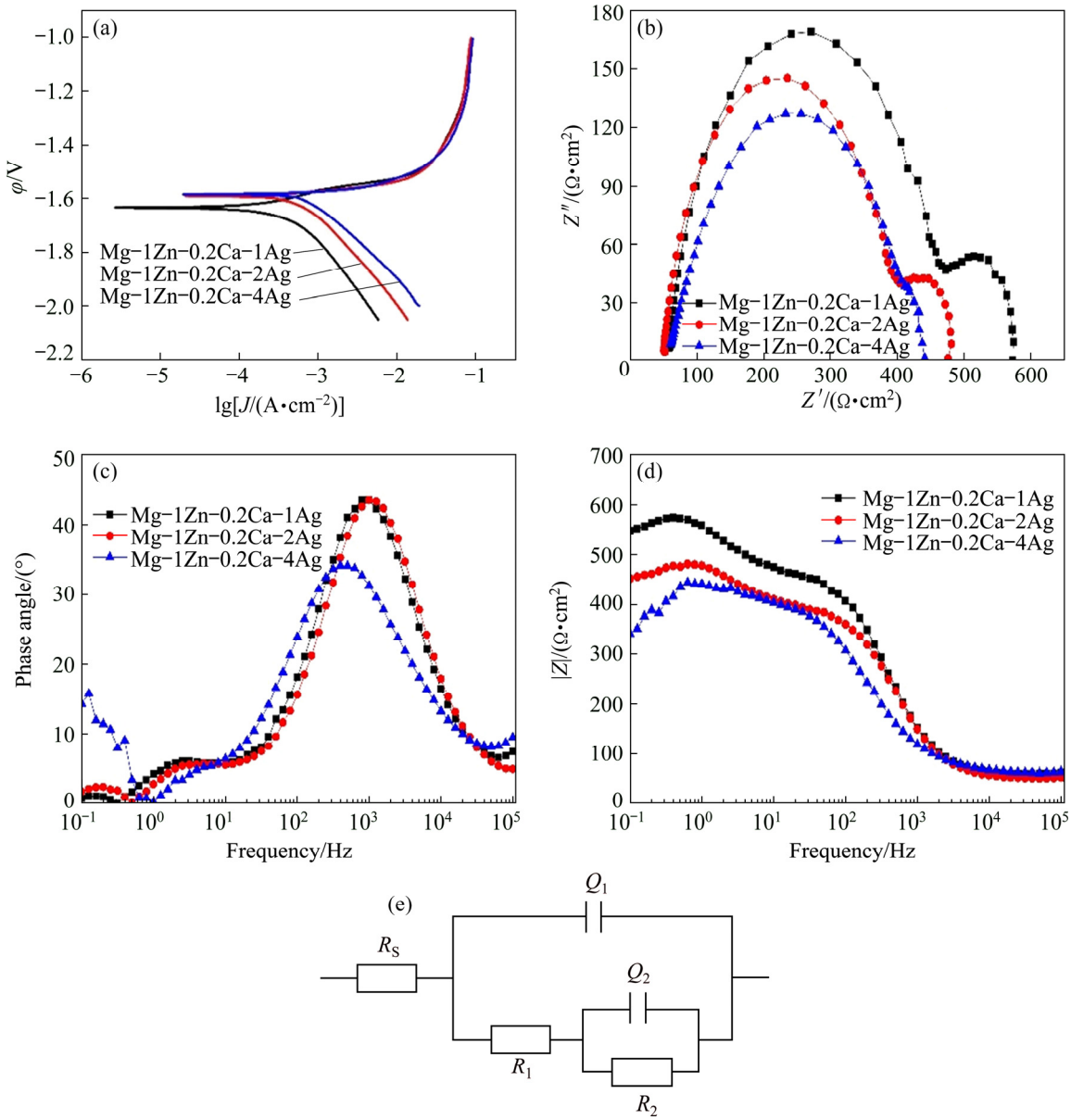

Fig. 9 Potentiodynamic polarization testing results (a), Nyquist (b) and Bode (c, d) plots of Mg−1Zn−0.2Ca−*x*Mg alloy wires and equivalent circuit model (e)

Table 2 Electrochemical results of Mg−1Zn−0.2Ca−*x*Ag alloy wires in SBF

Alloy	φ_{corr}/V	J_{corr}/(μA·cm^{-2})	β_c/mV
Mg−1Zn−0.2Ca−1Ag	−1.618	557.25	141.22
Mg−1Zn−0.2Ca−2Ag	−1.515	635.38	128.60
Mg−1Zn−0.2Ca−4Ag	−1.536	882.15	107.99

electrolyte [34,37]. The EIS spectra of Mg−Zn−Ca−Ag alloys are characteristic of one capacitive loop at high frequency and one at low frequency observed in SBF shown in Fig. 9(a). The capacitive loop of Mg−1Zn−0.2Ca−4Ag alloy wire at low frequency in SBF becomes less distinct, which can be attributed to local active dissolution and loose corrosion products formed on the surface of the wire [38]. The diameter of capacitive loop changes during the immersion period and decreases to the minimum value when Ag content is up to 4 wt.%, demonstrating that the corrosion resistance related to the composition of alloys decreases. The phase angle indicates the difficulty of charge transfer in corrosion process which is illustrated in Fig. 9(c). The peak value of Mg−1Zn−0.2Ca−4Ag alloy wire is significantly smaller than that of Mg−1Zn−0.2Ca−1Ag and Mg−1Zn−0.2Ca−2Ag alloy wires, demonstrating that charge transfer of Mg−1Zn−0.2Ca−4Ag alloy wire during corrosion is easier.

The impedance modulus $|Z|$ of Mg−1Zn−0.2Ca−xAg alloy wires in SBF solution are displayed in Fig. 9(d). The declining $|Z|$ value of Mg−1Zn−0.2Ca−4Ag alloy, compared with that of Mg−1Zn−0.2Ca−1Ag and Mg−1Zn−0.2Ca−2Ag alloys in solution, demonstrates the poor corrosion resistance due to the increase of Ag content and thus reduces protective capacity of the alloys [39,40].

The EIS spectra in SBF are fitted using corresponding equivalent circuit model as shown in Fig. 9(e), where R_S represents the solution resistance; R_1 is the resistance of the corrosion product film; R_2 is the charge transfer resistance at the electrode/electrolyte interface; Q_1 and Q_2 are constant phase elements representing the capacities of the corrosion product film and the double-layer between the solution and the alloy, respectively. The fitting results are summarized in Table 3. R_S is relatively stable in aqueous solutions. The decrease of R_1 and relative increase of Q_1 indicate that the product film becomes more porous, and the decrease of R_2 may be resulted from more α-matrix contacting with aqueous solution due to the loose protective film with the Ag addition [41]. R (R=R_1+R_2) is introduced to investigate the corrosion resistance of the materials. The drastic decline of R value from 50.98 Ω·cm^2 for Mg−1Zn−0.2Ca−1Ag to 38.347 Ω·cm^2 for Mg−1Zn−0.2Ca−4Ag can be observed in SBF solution.

In general, the corrosion mechanisms can be explained as follows. When the Mg−Zn−Ca−Ag alloy wires are immersed in SBF solution, the electric double layers are formed at the interface between the alloy surfaces and electrolyte solution. Then, the surface especially adjacent to $Ag_{17}Mg_{54}$, is corroded firstly as a result of micro-anode accelerating role of the second phases. However, the addition of Ag element can improve the substrate potential certified by the φ_{corr} values in Table 2, and transform degradation to homogeneous corrosion instead of pitting corrosion, as revealed by TIE et al [28]. The $Mg(OH)_2$ film appears on the alloy surfaces, and induces a capacity resistance character of the corrosion product layer, which hinders further corrosion for the Mg−1Zn−0.2Ca−1Ag and Mg−1Zn−0.2Ca−2Ag alloy wires in particular. Nevertheless, chloride ion (Cl^-) in SBF, which deteriorates protective film during immersion, can permeate the protective film and destroy its integrity with the time increasing. The formation and dissolution of corrosion film can be represented by the following reactions [42−44]:

$$Mg=Mg^{2+}+2e \quad (2)$$

$$2H_2O+2e=H_2+2OH^- \quad (3)$$

$$Mg^{2+}+2OH^-=Mg(OH)_2 \quad (4)$$

$$Mg(OH)_2+Cl^-=MgCl_2+2OH^- \quad (5)$$

Moreover, the structural discontinuity between the crystal structure of oxide layer and the HCP lattice of magnesium results in the development of high compressive stress within the oxide layer [45]. Mismatched stress triggers the micro cracks in the protective layers, which will penetrate through the film and facilitate the reaction between $Ag_{17}Mg_{54}$ and Mg matrix. This is the reason why the Mg−1Zn−0.2Ca−1Ag and Mg−1Zn−0.2Ca−2Ag alloy wires have a more obvious loop at low frequency in the Nyquist plot shown in Fig. 9(b). For Mg−1Zn−0.2Ca−4Ag alloy wire, a mass of micro-galvanic cells are formed between the plentiful larger $Ag_{17}Mg_{54}$ and α-Mg matrix and even the $Mg(OH)_2$ film on the alloy surface with the corrosion developing can easily be ruined. The degradation rate of Mg−1Zn−0.2Ca−4Ag alloy wire develops so fast that there is nearly no time to keep the film integrated. Thus, the Mg−1Zn−0.2Ca−4Ag alloy wire has no apparent loop at low frequency and keeps the highest corrosion rate among all the alloys. Besides, the sequence of J_{corr} in the alloys keeps monotonicity as similar as the value of the R, modulus $|Z|$ and the phase angle from the EIS analysis. In summary, the rank order of corrosion resistance is Mg−1Zn−0.2Ca−1Ag > Mg−1Zn−0.2Ca−2Ag > Mg−1Zn−0.2Ca−4Ag using the electrochemical tools, which is consistent with the

Table 3 Fitting results of EIS plots

Alloy	R_S/(Ω·cm^2)	R_1/(Ω·cm^2)	Q_1/(F·cm^{-2})	R_2/(Ω·cm^2)	Q_2/(F·cm^{-2})
Mg−1Zn−0.2Ca−1Ag	5.69	41.44	3.819×10^{-5}	9.54	6.701×10^{-3}
Mg−1Zn−0.2Ca−2Ag	4.983	35.13	3.412×10^{-5}	7.914	6.518×10^{-3}
Mg−1Zn−0.2Ca−4Ag	5.908	37.6	1.904×10^{-4}	0.747	1.095×10^{-5}

results of mass loss and hydrogen evolution discussed before.

4 Conclusions

(1) The microstructure analysis indicates that Mg−Zn−Ca−Ag alloy wires are mainly composed of α-Mg matrix and spherical $Ag_{17}Mg_{54}$, and the second precipitates increase as the Ag content increases.

(2) The wires with different Ag contents exhibit a tensile strength of at least 313 MPa and an elongation of not less than 7%, demonstrating their outstanding mechanical properties and knotting test also proves their good formability. Especially, Mg−1Zn−0.2Ca−4Ag alloy exhibits the highest mechanical properties, i.e. an ultimate tensile strength of 334 MPa and an elongation of 8.6%. Thus Mg−1Zn−0.2Ca−4Ag alloy can exhibit the best combination of strength and corrosion resistance to meet the demands of the anastomotic nails.

(3) Microstructural features such as grain size and the amount and distribution of second phase of magnesium alloys have important influences on corrosion resistance. The second phase $Ag_{17}Mg_{54}$ has an obviously low potential against α-Mg matrix. The Mg−1Zn−0.2Ca−4Ag alloy has a fastest corrosion rate in SBF, because of the precipitation of a larger amount of $Ag_{17}Mg_{54}$ and the second phase with α-Mg matrix forms micro-galvanic corrosion cells which accelerates the corrosion rate and ruins the film of $Mg(OH)_2$. The rank order of corrosion resistance is Mg−1Zn−0.2Ca−1Ag > Mg−1Zn−0.2Ca−2Ag > Mg−1Zn−0.2Ca−4Ag in this study.

Acknowledgments

The authors are grateful for the financial supports from the National Natural Science Foundation of China (51671017 and 51971020), the Beijing Municipal Natural Science Foundation, China (2202033), Beijing Laboratory of Metallic Materials and Processing for Modern Transportation, China, the Fundamental Research Funds for the Central Universities, China (FRF-IC-19-015), the Major State Research and Development Program of China (2016YFB0300801), and the Opening Research Fund of State Key Laboratory for Advanced Metals and Materials, China (2018-Z04).

References

[1] LIU Chen, REN Zheng, XU Yong-dong, PANG Song, ZHAO Xin-bing, ZHAO Ying. Biodegradable magnesium alloys developed as bone repair materials: A review [J]. Scanning, 2018, 2018: 9216314.

[2] SEITZ J, UTERMOHLEN D, WULF E, KLOSE C, BACH F. The manufacture of resorbable suture material from magnesium-drawing and stranding of thin wires [J]. Advanced Engineering Materials, 2011, 13(12): 1087−1095.

[3] XU De-xing, YANG Chang-lin, ZHAO Kang-ning, LI Hong-xiang, ZHANG Ji-shan. Interfacial microstructure and mechanical behavior of Mg/Cu bimetal composites fabricated by compound casting process [J]. Transactions of Nonferrous Metals Society of China, 2019, 29(6): 1233−1241.

[4] TESAŘ K, BALIK K, SUCHARDA Z, JAGER A. Direct extrusion of thin Mg wires for biomedical applications [J]. Transactions of Nonferrous Metals Society of China, 2020, 30(2): 373−381.

[5] ZENG R C, DIETZEL W, WITTE F, HORT N, BLAWERT C. Progress and challenge for magnesium alloys as biomaterials [J]. Advanced Engineering Materials, 2008, 10(8): B3−B14.

[6] HAUDE M, INCE H, ABIZAID A, TOELG R, LEMOS P A, von BIRGELEN C, CHRISTIANSEN E H, WIJNS W, NEUMANN F, KAISER C, EECKHOUT E, LIM S T, ESCANED J, GARCIAGARCIA H M, WAKSMAN R. Safety and performance of the second-generation drug-eluting absorbable metal scaffold in patients with de-novo coronary artery lesions (BIOSOLVE-II): 6 month results of a prospective, multicentre, non-randomised, first-in-man trial [J]. The Lancet, 2016, 387(10013): 31−39.

[7] VIRTANEN S. Biodegradable Mg and Mg alloys: Corrosion and biocompatibility [J]. Materials Science and Engineering B, 2011, 176(20): 1600−1608.

[8] SONG M S, ZENG R C, DING Y F, LI R W, EASTON M, COLE I S, BIRBILIS N, CHEN X B. Recent advances in biodegradation controls over Mg alloys for bone fracture management: A review [J]. Journal of Materials Science & Technology, 2019, 35(4): 535−544.

[9] ABOUDZADEH N, DEHGHANIAN C, SHOKRGOZAR M A. In vitro degradation and cytotoxicity of Mg−5Zn−0.3Ca/*n*HA biocomposites prepared by powder metallurgy [J]. Transactions of Nonferrous Metals Society of China, 2018, 28(9): 1745−1754.

[10] LIM C B B, GOLDIN R D, DARZI A, HANNA G B. Characterization of materials eliciting foreign body reaction in stapled human gastrointestinal anastomoses [J]. British Journal of Surgery, 2008, 95(8): 1044−1050.

[11] KIRKLAND N T, BIRBILIS N, STAIGER M P. Assessing the corrosion of biodegradable magnesium implants: A critical review of current methodologies and their limitations [J]. Acta Biomaterialia, 2012, 8(3): 925−936.

[12] SUN Liu-xia, BAI Jing, XUE Feng, TAO Li, CHU Cheng-lin, MENG Jiao. Exceptional texture evolution induced by multi-pass cold drawing of magnesium alloy [J]. Materials & Design, 2017, 135: 267−274.

[13] YAN Kai, SUN Jia-peng, BAI Jing, LIU Huan, HUANG Xin, JIN Zhao-yang, WU Yu-na. Preparation of a high strength and high ductility Mg−6Zn alloy wire by combination of ECAP and hot drawing [J]. Materials Science and Engineering A, 2019, 739: 513−518.

[14] CHEN Wen-zhen, ZHANG Wen-zhi, CHAO Hong-ying, ZHANG L X, WANG E. Influence of large cold strain on the microstructural evolution for a magnesium alloy subjected to multi-pass cold drawing [J]. Materials Science and Engineering A, 2015, 623: 92−96.

[15] CAI Hong, ZHANG Yue, LI Xuan, MENG Jiao, XUE Feng, CHU Cheng-lin, TAO Li, BAI Jing. Self-reinforced biodegradable Mg−2Zn alloy wires/polylactic acid composite for orthopedic implants [J]. Composites Science and Technology, 2018, 162: 198−205.

[16] ZHANG Shao-xiang, ZHANG Xiao-nong, ZHAO Chang-lin, LI Jia-nan, SONG Yang, XIE Chao-ying, TAO Hai-rong, ZHANG Yan, HE Yao-hua, JIANG Yao, BIAN Yu-jun. Research on an Mg−Zn alloy as a degradable biomaterial [J]. Acta Biomaterialia, 2010, 6(2): 626−640.

[17] YAN Jun, CHEN Yi-gang, YUAN Qing-ling, YU Song, QIU Wen-cai, YANG Cheng-guang, WANG Zhi-gang, GONG Jian-feng, AI Kai-xing, ZHENG Qi, LI Jia-nan, ZHANG Shao-xiang, ZHANG Xiao-nong. Comparison of the effects of Mg−6Zn and titanium on intestinal tract in vivo [J]. Journal of Materials Science: Materials in Medicine, 2013, 24(6): 1515−1525.

[18] LI Hong-xiang, QIN Shi-kai, MA Ying-zhong, WANG Jian, LIU Yun-jin, ZHANG Ji-shan. Effects of Zn content on the microstructure and the mechanical and corrosion properties of as-cast low-alloyed Mg−Zn−Ca alloys [J]. International Journal of Minerals Metallurgy and Materials, 2018, 25(7): 800−809.

[19] LI Hong-xiang, QIN Shi-kai, YANG Chang-lin, MA Ying-zhong, WANG Jian, LIU Yun-jin, ZHANG Ji-shan. Influence of Ca addition on microstructure, mechanical properties and corrosion behavior of Mg−2Zn alloy [J]. China Foundry, 2018, 15(5): 363−371.

[20] MA Ying-zhong, YANG Chang-lin, LIU Yun-jin, YUAN Fu-song, LIANG Shan-shan, LI Hong-xiang, ZHANG Ji-shan. Microstructure, mechanical, and corrosion properties of extruded low-alloyed Mg−*x*Zn−0.2Ca alloys [J]. International Journal of Minerals Metallurgy and Materials, 2019, 26(10):1274−1284.

[21] NAMI B, MIRESMAEILI S M, JAMSHIDI F, KHOUBROU I. Effect of Ca addition on microstructure and impression creep behavior of cast AZ61 magnesium alloy [J]. Transactions of Nonferrous Metals Society of China, 2019, 29(10): 2056−2065.

[22] SUN Yu, ZHANG Bao-ping, WANG Yin, GENG Lin, JIAO Xiao-hui. Preparation and characterization of a new biomedical Mg−Zn−Ca alloy [J]. Materials & Design, 2012, 34: 58−64.

[23] ABBASI E, MILANI M, S F A, KOUHI M, AKBARZADEH A, H T N, NIKASA P, JOO S W, HANIFEHPOUR Y, NEJATIKOSHKI K, SAMIEI M. Silver nanoparticles: Synthesis methods, bio-applications and properties [J]. Critical Reviews in Microbiology, 2014, 42(2): 173−180.

[24] SHOLKAMY E N, AHAMD M S, YASSER M M, ESLAM N. Anti-microbiological activities of bio-synthesized silver nano-stars by Saccharopolyspora hirsute [J]. Saudi Journal of Biological Sciences, 2019, 26(1): 195−200.

[25] ZHOU H, CHENG G M, MA X L, XU W Z, MATHAUDHU S N, WANG Q D, ZHU Y T. Effect of Ag on interfacial segregation in Mg−Gd−Y−(Ag)−Zr alloy [J]. Acta Materialia, 2015, 95: 20−29.

[26] MA Ying-zhong, WANG De-xin, LI Hong-xiang, YUAN Fu-song, YANG Chang-lin, ZHANG Ji-shan. Microstructure, mechanical and corrosion properties of novel quaternary biodegradable extruded Mg−1Zn−0.2Ca−*x*Ag alloys [J]. Materials Research Express, 2020, 7(1): 015414.

[27] LIU Yi, CHEN Xue-fei, WEI Kang, XIAO Li-rong, CHEN Bin, LONG Hai-bo, YU Yan-dong, HU Zhao-hua, ZHOU Hao. Effect of micro-steps on twinning and interfacial segregation in Mg−Ag alloy [J]. Materials, 2019, 12(8): 1307.

[28] TIE D, FEYERABEND F, HORT N, HOECHE D, KAINER K U, WILLUMEIT R, MUELLER W D. In vitro mechanical and corrosion properties of biodegradable Mg−Ag alloys [J]. Materials and Corrosion, 2014, 65(6): 569−576.

[29] LIU Z D, SCHADE R, LUTHRINGER B, HORT N, ROTHE H, MULLER S, LIEFEITH K, WILLUMEITROMER R, FEYERABEND F. Influence of the microstructure and silver content on degradation, cytocompatibility, and antibacterial properties of magnesium−silver alloys in vitro [J]. Oxidative Medicine and Cellular Longevity, 2017, 2017: 8091265.

[30] WANG J, ZHANG Y N, HUDON P, JUNG I, MEDRAJ M, CHARTRAND P. Experimental study of the phase equilibria in the Mg−Zn−Ag ternary system at 300 °C [J]. Journal of Alloys and Compounds, 2015, 639(639): 593−601.

[31] BAKHSHESHIRAD H R, HAMZAH E, FEREIDOUNILOTFABADI A, DAROONPARVAR M, YAJID M A M, MEZBAHULISLAM M, KASIRIASGARANI M, MEDRAJ M. Microstructure and bio-corrosion behavior of Mg−Zn and Mg−Zn−Ca alloys for biomedical applications [J]. Materials and Corrosion, 2014, 65(12): 1178−1187.

[32] TAKEUCHI A, INOUE A. Classification of bulk metallic glasses by atomic size difference, heat of mixing and period of constituent elements and its application to characterization of the main alloying element [J]. Materials Transactions, 2005, 46(12): 2817−2829.

[33] BENHAMU G, ELIEZER D, KAYA A A, NA Y G, SHIN K S. Microstructure and corrosion behavior of Mg−Zn−Ag alloys [J]. Materials Science and Engineering A, 2006, 435: 579−587.

[34] CHO D H, LEE B W, PARK J, CHO K M, PARK I M. Effect of Mn addition on corrosion properties of biodegradable Mg−4Zn−0.5Ca−*x*Mn alloys [J]. Journal of Alloys and Compounds, 2017, 695: 1166−1174.

[35] JAYALAKSHMI S, SANKARANARAYANAN S, KOH S P X, GUPTA M. Effect of Ag and Cu trace additions on the microstructural evolution and mechanical properties of

Mg−5Sn alloy [J]. Journal of Alloys and Compounds, 2013, 565: 56−65.

[36] WANG Li-qing, QIN Gao-wu, SUN Shi-neng, REN Yu-ping, SONG Li. Effect of solid solution treatment on in vitro degradation rate of as-extruded Mg−Zn−Ag alloys [J]. Transactions of Nonferrous Metals Society of China, 2017, 27(12): 2607−2612.

[37] CHANG Jian-wei, GUO Xing-wu, FU Peng-huai, PENG Li-ming, DING Wen-jiang. Effect of heat treatment on corrosion and electrochemical behaviour of Mg−3Nd−0.2Zn−0.4Zr (wt.%) alloy [J]. Electrochimica Acta, 2007, 52(9): 3160−3167.

[38] FENG Hui, LIU Shu-hong, DU Yong, LEI Ting, ZENG Rong-chang, YUAN Tie-chui. Effect of the second phases on corrosion behavior of the Mg−Al−Zn alloys [J]. Journal of Alloys and Compounds, 2017, 695: 2330−2338.

[39] BAKHSHESHIRAD H R, HAMZAH E, ISMAIL A F, AZIZ M, NAJAFINEZHAD A, DAROONPARVAR M. Synthesis and in-vitro performance of nanostructured monticellite coating on magnesium alloy for biomedical applications [J]. Journal of Alloys and Compounds, 2019, 773: 180−193.

[40] JAMESH M, KUMAR S, NARAYANAN T S N S. Corrosion behavior of commercially pure Mg and ZM21 Mg alloy in Ringer's solution – Long term evaluation by EIS [J]. Corrosion Science, 2011, 53(2): 645−654.

[41] SONG G L, UNOCIC K A. The anodic surface film and hydrogen evolution on Mg [J]. Corrosion Science, 2015, 98: 758−765.

[42] BAKHSHESHIRAD H R, IDRIS M H, ABDULKADIR M R, OURDJINI A, MEDRAJ M, DAROONPARVAR M, HAMZAH E. Mechanical and bio-corrosion properties of quaternary Mg−Ca−Mn−Zn alloys compared with binary Mg−Ca alloys [J]. Materials & Design, 2014, 53: 283−292.

[43] RAD H R B, IDRIS M H, KADIR M R A, FARAHANY S. Microstructure analysis and corrosion behavior of biodegradable Mg−Ca implant alloys [J]. Materials & Design, 2012, 33: 88−97.

[44] ZENG R C, ZHANG J, HUANG W J, DIETZEL W, KAINER K U, BLAWERT C, WEI K E. Review of studies on corrosion of magnesium alloys [J]. Transactions of Nonferrous Metals Society of China, 2006, 16: 763−771.

[45] ARGADE G R, PANIGRAHI S K, MISHRA R S. Effects of grain size on the corrosion resistance of wrought magnesium alloys containing neodymium [J]. Corrosion Science, 2012, 58: 145−151.

吻合钉用可降解四元 Mg−1Zn−0.2Ca−*x*Ag 合金丝材的显微组织、力学性能和腐蚀行为

马英中[1]，王德鑫[1]，李宏祥[1]，杨长林[2]，原福松[3]，张济山[1]

1. 北京科技大学 新金属材料国家重点实验室，北京 100083；
2. 西北工业大学 凝固技术国家重点实验室，西安 710072；
3. 北京大学口腔医院 口腔数字化中心，北京 100081

摘　要：研究吻合钉用 Mg−1Zn−0.2Ca−*x*Ag (*x*=1, 2, 4, %，质量分数)可降解镁合金丝材的显微组织、力学性能和腐蚀行为。通过 SEM、EDS、XRD 和 TEM 分析，发现合金主要由 Mg 基体和 $Ag_{17}Mg_{54}$ 相组成。拉伸和打结试验结果表明，该合金丝材具有优良的力学性能。特别是 Mg−1Zn−0.2Ca−4Ag 合金的力学性能最好，其极限抗拉强度为 334 MPa，伸长率为 8.6%。此外，根据质量损失实验和 SKPFM 结果，随着 Ag 含量的增加，Mg 基体与 $Ag_{17}Mg_{54}$ 相之间形成微电偶，镁合金丝材的腐蚀速率显著增加。该镁合金能在 28 d 内在体内完全降解，各项性能均能满足吻合钉的要求。

关键词：Mg−Zn−Ca−Ag 合金；可降解性；吻合钉；显微组织；力学性能；腐蚀行为

(Edited by Wei-ping CHEN)